Suppression of one-dimensional weak localization by band asymmetry

Kartikeya Arora, Rajeev Singh, and Pavan Hosur

Phys. Rev. B **108**, 064211 — Published 23 August 2023

DOI: 10.1103/PhysRevB.108.064211

Suppression of one-dimensional weak localization by band asymmetry

Kartikeya Arora and Rajeev Singh
Department of Physics, Indian Institute of Technology (Banaras Hindu University), Varanasi 221005, India

Pavan Hosur
Department of Physics and Texas Center for Superconductivity, University of Houston, Houston 77004, USA

We investigate disorder-induced localization in metals that break time-reversal and inversion symmetries through their energy dispersion, $\epsilon_k \neq \epsilon_{-k}$, but lack Berry phases. In the perturbative regime of disorder, we show that weak localization is suppressed due to a mismatch of the Fermi velocities of left and right movers. To substantiate this analytical result, we perform quench numerics on chains shorter than the Anderson localization length ξ – the latter computed and verified to be finite using the recursive Green's function method – and find a sharp rise in the saturation value of the participation ratio due to band asymmetry, indicating a tendency to delocalize. Interestingly, for weak disorder strength η, we see a better fit to the scaling behavior $\xi \propto 1/\eta^2$ for asymmetric bands than conventional symmetric ones.

I. INTRODUCTION

Weak localization (WL) refers to an enhanced tendency of electrons in a disordered potential to localize due to constructive quantum interference between pairs of time-reversed paths [1–6]. It serves as a precursor to Anderson or *strong* localization which refers to the true arrest of quantum diffusion of free electrons on a lattice [7]. Since its conception in the context of electrons in a metal, Anderson localization has been seen in light waves [8–10], ultrasound [11, 12], ultracold atoms [13–16], and more recently, digital quantum simulators such as those provided by IBMQ [17, 18].

The two regimes of localization are elegantly captured by the scaling theory of localization [1, 2, 19, 20]. Formulated as a renormalization group approach, it describes the scaling behavior of conductance in disordered systems via a scaling function that, in its simplest form, depends only on the conductance but has no explicit dependence on system size. Then, the physical conductance in the thermodynamic limit is given by the appropriate stable fixed point of the renormalization group flow. The results of this procedure depend sensitively on the dimensionality and symmetry class of the system [1, 19–23]. In three dimensions (3D), the scaling function has a zero of order unity in every symmetry class, which is an unstable fixed point that separates the localized and delocalized regimes at strong and weak disorder, respectively. The localized phase corresponds to Anderson's original prediction of localization in a disordered lattice. In 2D, the asymptotic behavior of the system depends delicately on its symmetries. If time-reversal symmetry ($\mathcal{T}$) is absent (unitary class) or present but bosonic ($\mathcal{T}^2 = 1$, orthogonal class), disorder is marginally relevant [1, 19, 20, 24]. Physically, this means infinitesimal disorder will eventually localize the system in the thermodynamic limit, but the localization length in practice can be astronomically large. This leads to striking experimental signatures such as a sharp, symmetric cusp in the magnetoconductance as the constructive interference is ruined by the Aharanov-Bohm phase of the magnetic field. In contrast, the presence of fermionic $\mathcal{T}$ ($\mathcal{T}^2 = -1$, symplectic class), pertinent to metals with strong spin-orbit coupling, causes disorder to be marginally irrelevant, leads to weak anti-localization, and allows metallicity to survive up to the thermodynamic limit at extremely weak disorder [24]. Experimentally, weak anti-localization manifests as a peak instead of a cusp in the magnetoresistance. Finally in 1D, disorder is relevant and the scaling function is always negative, which physically implies localization for infinitesimal disorder in any symmetry class.

Most of our current understanding of metallic physics is based on the presence of at least one of inversion ($\mathcal{I}$) and time-reversal ($\mathcal{T}$) symmetries, as bulk metals that break both symmetries, i.e., noncentrosymmetric, magnetic metals, are extremely rare. The symmetries govern key macroscopic properties of metals via microscopic processes such as Cooper pairing and elastic backscattering, pertinent to superconductivity and localization, respectively. On the other hand, largely thanks to the poor screening of electromagnetic fields, lower dimensional systems allow phenomena that are suppressed or forbidden in bulk materials. For instance, $\mathcal{T}$- and $\mathcal{I}$-breaking enable a host of exotic superconducting behaviors either in systems that are (quasi)-1D or the phenomena themselves have a directionality. These include Majorana fermions in nanowires [25–29], superconducting [30–41] and Josephson diode effects [42–50], and spontaneous su-

percurrents at equilibrium [51–53]. This immediately raises the question, "what are the consequences of $\mathcal{T}$- and $\mathcal{I}$-breaking on the *localization* properties of 1D metals?"

In this work, we address this question in the simplest scenario: 1D metals of spinless electrons with an asymmetric dispersion, $\epsilon_k \neq \epsilon_{-k}$, in a disordered chemical potential. We refer to such metals as band asymmetric metals (BAMs) and stress that they are the generic low-energy theory of 1D metals that lack any symmetry; several examples are given in Appendix A. This problem technically belongs to the unitary class; however, it differs from the usual problem of localization in this class where disorder breaks $\mathcal{T}$ but the underlying metal does not, resulting in preserved $\mathcal{T}$ on average. In contrast, the current problem violates $\mathcal{T}$ on average too as $\mathcal{T}$ is already broken by the parent metal. Therefore, this system is conceptually closer to a metal in a magnetic field than to one with magnetic impurities. We study both weak and strong localization in 1D BAMs and find that the former contains a new physical regime while the latter enjoys a localization length that grows parametrically with band asymmetry.

In Section II, we discuss the WL correction to the conductivity in 1D BAMs which is followed by the discussion of quench numerics and recursive Green's function method calculations in Section III and is concluded by a discussion on possible avenues for experimental realizations in Section IV. The appendices contain the discussion of some physical models with $\mathcal{T}$- and $\mathcal{I}$- breaking perturbations, the details of the conductivity correction calculations, and the specifics of the recursive Green's function (RGF) method.

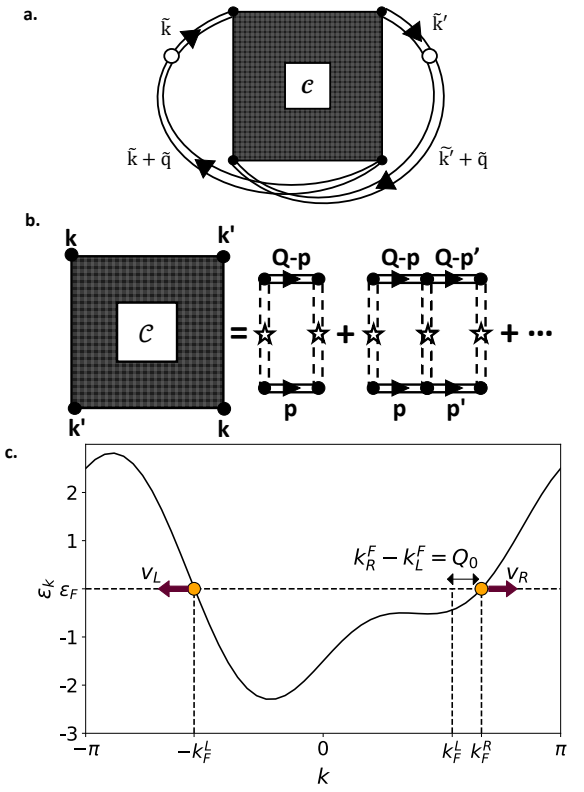

Figure 1. (a) Feynman diagrams representing the polarization bubble for the maximally crossed (Langer-Neal) diagram, where $\mathcal{C}$ is the resummed Cooperon propagator represented diagrammatically by a sum of parallel impurity lines in (b). Here, $\tilde{k} \equiv (k, i\nu_n)$ and $\tilde{k}' \equiv (k', i\nu_n + i\omega_n)$ label the top incoming and outgoing lines while $\tilde{q} \equiv (q, i\omega_n)$ is the difference between their frequency/momentum. (c) Representative asymmetric band showing the Fermi points and highlighting the difference in the speeds of the left and right movers.

II. GENERAL CONDUCTIVITY CORRECTION

Our main result is a new regime of WL in 1D BAMs. Specifically, we show that the WL correction to the conductivity in 1D BAMs is given by:

$$\sigma^{\mathrm{WL}} \approx -\frac{e^2}{\hbar}\frac{2\pi v\tau_0}{\sqrt{\frac{l}{l_\phi}+\frac{\delta v^2}{4v^2}}}. \tag{1}$$

for $l/l_\phi, |\delta v|/v \ll 1$, where $v = (v_L + v_R)/2$ is the average speed of the left and right movers, $\delta v = v_R - v_L$ is the difference in speeds, l is the mean free path, l_ϕ is a phenomenological phase coherence length that is typically governed by inelastic scattering and thermal decoherence, and τ_0 is the quasiparticle lifetime calculated in the Born approximation. We have assumed a single pair of counterpropagating modes for simplicity. Eq. (1) shows two distinct regimes: for $\sqrt{\frac{l}{l_\phi}} \ll \frac{|\delta v|}{2v}$ and $\sqrt{\frac{l}{l_\phi}} \gg \frac{|\delta v|}{2v}$, dephasing is dominated by band asymmetry and inelastic scattering, respectively. Thus, symmetric metals with $\delta v = 0$ fall in the latter regime and have $\sigma^{\mathrm{WL}} \propto -\sqrt{l_\phi}$ [54], which diverges at zero temperature in the absence of inelastic scattering processes. Intuitively, right and left moving waves at a given speed have equal and opposite momenta. Therefore, they form a perfect standing wave and enhance localization. In contrast, if band asymmetry is large enough [Fig. 1 (c)], the standing wave heuristically melts into an interference pattern with net drift. Eq. (1) predicts this for $\sqrt{\delta v/v} \gg l/l_\phi$; then σ^{WL} remains finite as l_ϕ diverges and depends on disorder only through τ_0.

To arrive at Eq. (1), we begin by assuming random chemical potential quenched disorder and considering the effect of band asymmetry on $\tau_0^{-1} =$

$2\mathrm{Im}\Sigma(i0^+)$ in the Born approximation, where $\Sigma(z)$ is the complex frequency dependent self-energy. Although the BAM has unequal Fermi momenta for left and right movers, $|k_F^L| \neq |k_F^R|$ [Fig. 1 (c)], τ_0 depends on the band structure only through the density of states at the Fermi level. As a result, we find that it changes quantitatively, but not qualitatively, as the bands turn asymmetric. Physically, this means band asymmetry does not qualitatively affect classical transport, i.e., transport in the regime where quantum interference effects vanish and probabilities rather than amplitudes for different Feynman paths add. Thus, one must transcend the Born approximation and consider appropriate vertex corrections to see the qualitative effects of band asymmetry.

In a $\mathcal{T}$-symmetric system, the vertex corrections that survive disorder-averaging consist of maximally crossed diagrams, illustrated in Fig. 1 (a,b). Thus, we evaluate the polarization bubble with these corrections following standard procedure [54, 55] to obtain σ^{WL}; see Appendix B for full details of the calculation. When computed for metals under a small orbital magnetic field, these corrections yield the well-known experimental signatures of WL in magnetoresistance. In the present context, fortunately, the calculation is simpler since band asymmetry is a non-singular perturbation unlike an orbital magnetic field. In particular, all momentum integrals here can be elegantly done by contour methods once we note that the integrals are dominated by regions near the Fermi points and linearize the dispersion around these points. Moreover, the dominant contributions to WL are captured by the retarded-advanced Cooperon propagator since the phenomenon effectively arises from interference between forward and backward time evolution of the electron wavefunction. Under the linear approximation, we find the retarded-retarded Cooperon propagator to exactly vanish. Linearization also naturally introduces the Fermi velocities $v_{L,R}$ into the calculation and lets us package the band asymmetry into a single dimensionless parameter, $\delta v/2v = (v_R - v_L)/(v_L + v_R)$. Finally, we resum the Dyson series for the Cooperon propagator and calculate the polarization bubble for conductivity to obtain σ^{WL}. Along the way, we include Markovian inelastic scattering into the calculation via a phenomenological phase decoherence probability e^{-l/l_ϕ} between elastic scattering events. This yields the result, Eq. (1), for $l \ll l_\phi$ and $\delta v \ll v$.

The dependence of σ^{WL} on band asymmetry only through δv indicates that the above phenomena appear in a wide range of physical systems. In Appendix A, we describe several systems with $\mathcal{T}$- and $\mathcal{I}$- breaking perturbations, some of which are dynamically tunable and have seen experimental realizations, where we expect a suppression of WL. In the next section, we focus on a lattice model and study localization in it numerically.

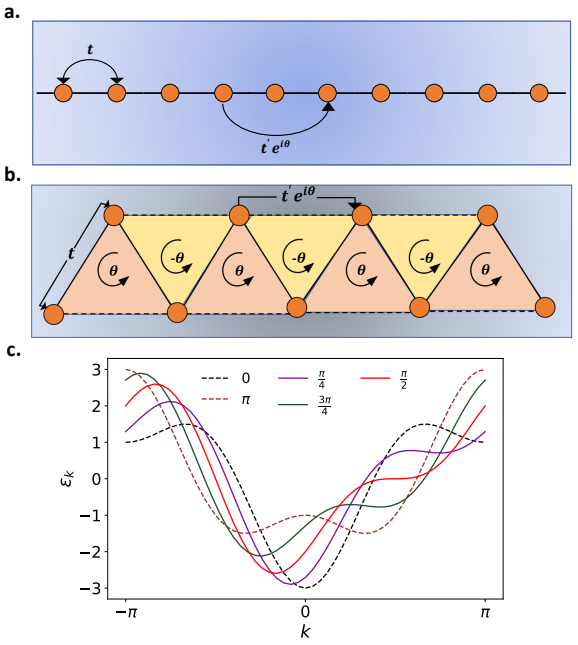

Figure 2. (a) A schematic representation of the 1D tight-binding model with real NN and complex NNN hopping. (b) Zigzag chain representation of the same model with alternating flux passing through adjacent triangles. (c) Graphical representation of the dispersion relation ϵ_k. Symmetric cases ($\theta = 0$ and $\theta = \pi$) and the asymmetric cases are represented by dashed and solid lines respectively.

III. NUMERICS ON ZIGZAG CHAIN

To substantiate the analytics, we study localization numerically on a tight-binding lattice model of spinless fermions [Fig. 2] described by

$$H = -t\sum_i c_i^\dagger c_{i+1} - t'e^{i\theta}\sum_i c_i^\dagger c_{i+2} + h.c. + \sum(\varepsilon_i - \mu)c_i^\dagger c_i, \quad (2)$$

where c_i and $c_i^\dagger$ are fermionic annihilation and creation operators at the lattice site 'i'. Also, t, t', θ, μ, and ε_i represent the nearest neighbor (NN) hopping strength, next-nearest neighbor (NNN) hopping strength, $\mathcal{T}$- and $\mathcal{I}$-breaking hopping phase, chemical potential, and the on-site disorder potential respectively. The dispersion in the absence of disorder is

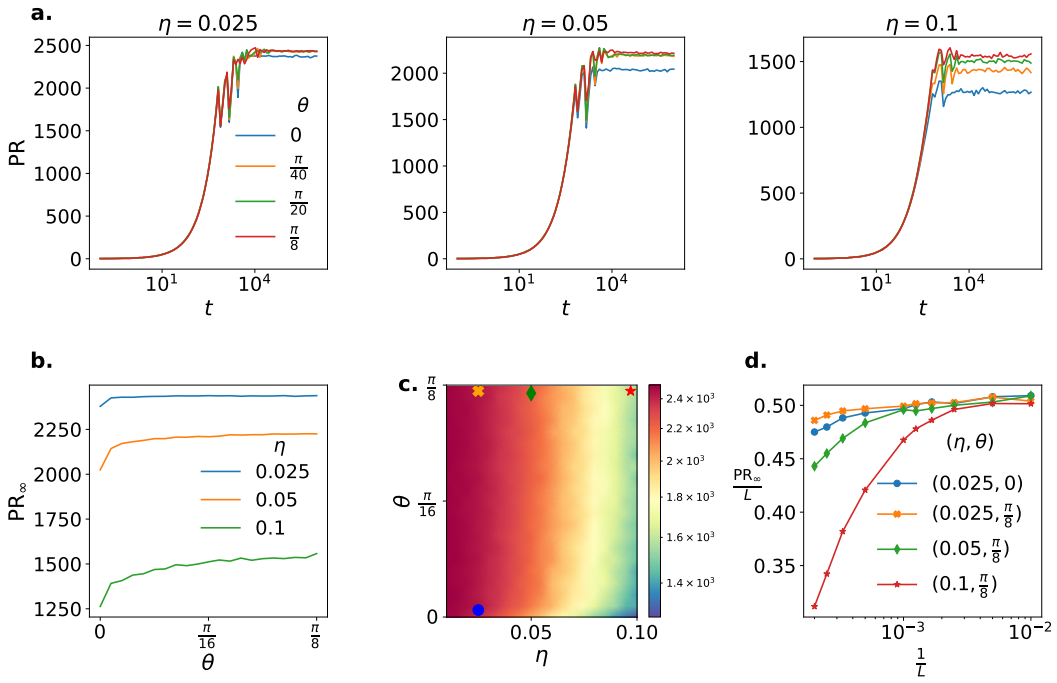

Figure 3. PR saturation with time for a system with $L = 5000$. (a) Time evolution of PR up to $t = 10^6$ for various θ, for a given η. (b) The long-time saturation value of PR, PR_∞, as a function of θ for various η. (c) Color plot showing the variation of PR_∞ with θ and η. (d) Finite-size scaling behavior of $\frac{\mathrm{PR}_\infty}{L}$ vs $\frac{1}{L}$ up to $L = 5000$ for some (η, θ) pairs marked in (c).

$$\epsilon_k = -2[t\cos(k) + t'\cos(2k + \theta)] - \mu, \qquad (3)$$

which shows band asymmetry for generic values of $\theta \neq 0, \pi$ [Fig. 2 (c)].

This model can also be viewed as a zigzag chain with triangular plaquettes [Fig. 2 (b)]. The NN hopping terms form the two sides of the triangles and NNN ones are across the bases. These triangular plaquettes have a total phase of $\pm\theta$ associated with them corresponding to the total phase picked up by a particle while hopping anti-clockwise along the edges. As we can see in Fig. 2 (b), adjacent triangles have opposite fluxes passing through them. However, we note that despite having a zigzag chain representation, the system has a 1-site unit cell and H is invariant under unit translation, $i \to i+1$. Throughout this paper, we consider $t = -1$, $t' = -0.5$, $\mu = -1$, and draw ε_i from a uniform distribution $[-\eta, \eta]$.

As a first diagnostic tool, we calculate the participation ratio (PR) defined as

$$\mathrm{PR} = \frac{1}{\sum_i |\psi_i|^4}, \qquad (4)$$

for a tight-binding wavefunction ψ. It is a measure of the number of states a particle is distributed over. For a particle localized on only one site, PR = 1, while a particle evenly distributed over L sites has PR = L. In general, a finite (vanishing) value of PR/L as $L \to \infty$ indicates delocalization (localization).

To study localization in our system, we numerically calculate the spread of wavefunctions starting from one that is localized on two neighboring sites, $\frac{|i\rangle + |i+1\rangle}{\sqrt{2}}$, $|i\rangle$ being the state corresponding to the particle localized on site 'i'. We have chosen this particular initial condition because its energy lies at the Fermi level for $\mu = -1$ and the effect of the suppression of weak localization is seen prominently at finite μ. We choose the sites in the middle of the chain but the location does not matter as we are using periodic boundary conditions in all our quantum quench calculations. We evolve the system up to $t = 10^6$ and perform a disorder average of 100 disorder realizations in most cases.

In Fig. 3 (a), we present the time evolution of PR for different η and θ in a system with $L = 5000$. The wavefunction of the particle starting in the middle of the lattice spreads over the system initially, resulting in an increase in PR with time. However, the spread does not continue indefinitely and PR saturates after some time. Increasing η reduces the saturation value of PR, which is consistent with WL;

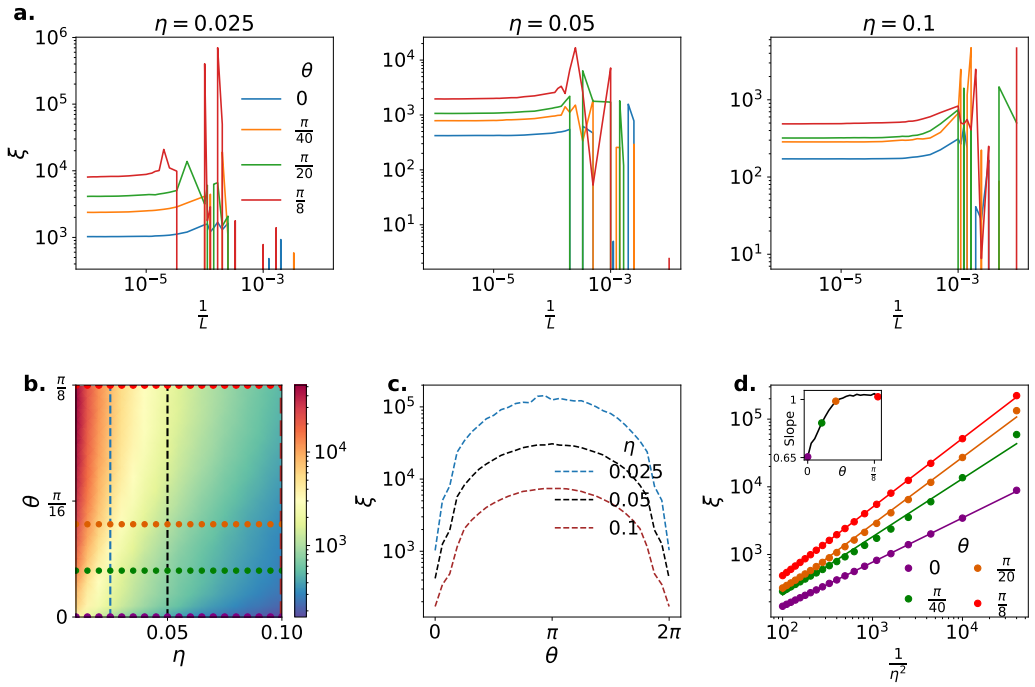

Figure 4. Localization length (ξ) calculations using recursive Green's function method up to $L = 10^6$. (a) Variation of ξ with θ for a given η as a function of $\frac{1}{L}$. (b) Color plot showing the variation of ξ with θ and η. (c) ξ as a function of θ for various η. (d) ξ as a function of $\frac{1}{\eta^2}$ for various θ. The dots represent the simulation data and the solid lines represent the power law fit. Inset shows the slope approaching 1 as θ increases.

however, a non-zero θ suppresses this effect resulting in a higher PR saturation value compared to the symmetric case [Fig 3 (c)]. We note that the suppression of WL increases monotonically and rapidly as θ increases away from 0 [Fig. 3 (b)]. We then perform finite size scaling of PR saturation values for various (θ, η) pairs. For small L, the PR increases linearly with L. As we argue below, this is because the localization length $\xi > L$ at these system sizes. However, $\frac{\mathrm{PR}_\infty}{L}$ decreases as we go towards larger L [Fig. 3 (d)], suggesting that 1D free-fermions systems might localize in the thermodynamic limit at arbitrarily small disorders even in the presence of band asymmetry.

The last statement is difficult to check using exact diagonalization for very weak disorder as ξ can be much larger than the system sizes this method can access. Fortunately, iterative algorithms such as transfer matrix [56] and recursive Green's function (RGF) method [57–59] exist which can access significantly larger system sizes. Thus, we complement our quench numerics by explicitly computing ξ using the RGF method. We explore various η and θ and system sizes up to $L = 10^6$, and average over 100 realizations. The details of RGF method for our system are presented in Appendix C.

We choose the Fermi energy for $\mu = -1$ as before to see the suppression of WL prominently. In Fig. 4 (a), we present the iterations of the RGF method calculations as a function of system size. After some fluctuations at small sizes, ξ clearly saturates to a constant value that defines the localization length in the thermodynamic limit for that particular (θ, η) pair. Fig. 4 (b) presents ξ as a function of both η and θ while Fig. 4(c,d) show cuts through this plot. For a particular η, ξ increases monotonically with increasing θ [Fig. 4 (c)] and decreases with increasing η [Fig. 4 (d)]. We see in Fig. 4 (c) that asymmetry increases ξ but shows signs of saturation rather than divergence, suggesting that the system is still localized.

In the regime of weak η and $\theta = 0$, perturbation theory [1, 60] predicts $\xi \propto \frac{1}{\eta^2}$. By employing similar arguments using Green function $G(E) = \int_k (E - \epsilon_k)^{-1}$ for $\theta \neq 0$, we get

$$\frac{1}{\xi} = -\frac{\eta^2}{12} \int^E G \frac{dG}{dE}, \tag{5}$$

where

$$\int^{E} G\frac{dG}{dE} = -\int^{E}\int_{k,k'} \frac{1}{E-\epsilon_k}\frac{1}{(E-\epsilon_{k'})^2} \quad (6)$$

$$= -\int_{k,k'} A_{k,k'}\ln(E-\epsilon_k) + \frac{B_{k,k'}}{E-\epsilon_{k'}}, \quad (7)$$

Provided the above integral is finite or properly regularized, the scaling behaviour $\xi \propto \frac{1}{\eta^2}$ holds true even for finite values of θ. We have verified this relationship between ξ and $\frac{1}{\eta^2}$ by performing a power law fit (solid lines) on the simulation data points (dots) [Fig. 4 (d)], where we observe the slope approaching 1 as θ increases [Fig. 4 (d) (inset)]. Since the scaling $\xi \propto \frac{1}{\eta^2}$ is well-known at $\theta = 0$ in the thermodynamic limit [1, 60], the deviation from this scaling is presumably due to finite size effects. This suggests that finite size effects, surprisingly, are smaller for $\theta \neq 0$.

PR and ξ both measure the degree of localization in a system, with PR quantifying the number of sites the wavefunction is spread over and ξ being the characteristic length scale over which the wave function decays. Therefore, we observe consistent trends in PR and ξ with varying η and θ. Notably, the RGF method calculations yield large values of ξ for certain parameters, surpassing the system size used in exact diagonalization. It is important to note here that these calculations correspond to two different regimes. The analytical result [Eq. (1)] is valid, and the PR calculations [Fig. 3] are done in the regime $\xi > L$ where a finite system is delocalized, whereas the RGF method calculations [Fig. 4] are performed in the regime $L > \xi$ which is smoothly connected to the thermodynamic limit. The trends in these numerical calculations align with the analytical result [Eq. (1)] that the conductivity increases due to asymmetry, though a finite ξ [Fig. 4] implies that the conductivity is 0 by definition in the thermodynamic limit.

IV. EXPERIMENTS

The suppression of localization due to band asymmetry can be probed in 1D metallic wires with Rashba spin-orbit coupling using a magnetic field. As described in Appendix A, the dispersion is symmetric in the absence of a magnetic field due to $\mathcal{T}$. A weak magnetic field will break $\mathcal{T}$, turn the bands asymmetric, and should enhance the conductivity. We emphasize that the enhancement in 1D is due to the Zeeman effect of the magnetic field, and is distinct from the usual suppression of WL due to the Aharanov-Bohm effect of an orbital field in 2D, 3D and even in 1D wires with a finite width [61, 62].

Concrete realizations of our model [Fig. 2] may also be achieved in synthetic [63] and optical [64] lattices, which offer high tunability of hopping amplitudes, disorder and fluxes using artificial gauge fields. Moreover, unlike solids, these platforms naturally lack phonons and uncontrolled disorder. With increasing flux as illustrated in Fig. 2, we predict a greater spread of an initially local wavefunction. In particular, the localization length extracted from the long-time density profiles should increase as the flux increases. While the Aharanov-Bohm flux plays a key role in this realization, its main role is to break the $k \to -k$ symmetry of the bands. Indeed, the average flux is zero, which distinguishes it from usual studies of WL in uniform magnetic fields in solid state systems.

V. CONCLUSIONS

We have shown that in 1D metals where time reversal and inversion symmetry are broken, dubbed band asymmetric metals, weak localization is suppressed due to the asymmetry in velocities of left and right movers. Heuristically, the formation of perfect standing waves due to quantum interference between time-reversed paths, leading to weak localization, is disrupted due to this asymmetry. The analytical results are validated by the numerical calculations of the participation ratio and localization length such that there is an increase in conductivity, participation ratio, and localization length with increasing band asymmetry, indicating a tendency to delocalize. Metallic nanowires with strong spin-orbit coupling and tunable synthetic and optical lattices with controlled disorders may be convenient platforms for experimentally investigating the impact of band asymmetry on the localization properties of disordered systems.

ACKNOWLEDGMENTS

P.H. was supported by the Department of Energy under grant no. DE-SC0022264. P.H. would like to thank Pouyan Ghaemi, Joseph Maciejko, and Hridis Pal for useful discussions. We acknowledge the National Supercomputing Mission (NSM) for providing computing resources of 'PARAM Shivay' at the Indian Institute of Technology (BHU), Varanasi, which is implemented by C-DAC and supported by the Ministry of Electronics and Information Technology (MeitY) and Department of Science and Technology (DST), Government of India. Some of the calculations have been performed using the Quspin library [65, 66].

Appendix A: Models and realizations

Here, we discuss three physical models with $\mathcal{T}$- and $\mathcal{I}$- breaking perturbations and calculate the asymmetry in speeds of left and right movers to leading order.

1. Zigzag chain

Considering the zigzag chain dispersion relation [Eq. (3)], for the symmetric case ($\theta = 0, \pi$) we find equal (in magnitude) and opposite (in direction) Fermi momenta

$$\pm k_F = \pm \begin{cases} \cos^{-1}\left(\frac{-2t+\sqrt{4t^2-16t'(\mu-2t')}}{8t'}\right) & \theta = 0 \\ \cos^{-1}\left(\frac{2t-\sqrt{4t^2+16t'(\mu+2t')}}{8t'}\right) & \theta = \pi \end{cases}, \tag{A1}$$

and equal Fermi speeds $v_R = -v_L \equiv v_F$ where

$$v_F = \left|2t \sin k_F + 4t' \sin 2k_F\right|. \tag{A2}$$

The perturbative correction due to small asymmetry θ to the leading order breaks $\mathcal{T}$and $\mathcal{I}$ symmetries to give $k_F^{R/L} = k_F \pm \delta$, where

$$\delta = \frac{-2t' \cos k_F}{t + 4t' \cos k_F}\theta, \tag{A3}$$

and

$$v_{R/L} = v_F \mp \frac{4tt' \sin^2 k_F}{t + 4t' \cos k_F}\theta, \tag{A4}$$

showing the difference in the magnitude of Fermi speeds, $\delta v \propto \theta$.

2. Cubic perturbation

For a continuum model with a cubic perturbation, the dispersion relation is given by

$$\epsilon_{cubic} = \frac{k^2}{2m} + \alpha k^3 + \beta k^4 - \mu, \tag{A5}$$

where αk^3 is the $\mathcal{T}$- and $\mathcal{I}$- breaking perturbation and βk^4 with $\beta > 0$ keeps ϵ_{cubic} positive in the limit $k \to \pm\infty$. We treat the quadratic and quartic terms in the dispersion as the unperturbed system and calculate the correction due to the cubic term. Similar to the zigzag chain, the symmetric case ($\alpha = 0$) has equal and opposite Fermi momenta

$$\pm k_F = \pm\sqrt{\frac{-1 + \sqrt{1 + 16\mu\beta m^2}}{4m\beta}} \tag{A6}$$

and equal Fermi speeds

$$v_F = \frac{k_F}{m} + 4\beta k_F^3 \tag{A7}$$

The cubic perturbation gives $k_F^{R/L} = k_F \pm \delta$, where $\delta = -\alpha k_F^2 m$ to leading order, and

$$v_{R/L} \approx v_F \pm 2k_F^2 \left[1 - \frac{6\beta k_F^2}{m}\right]\alpha, \tag{A8}$$

resulting in the difference in the magnitude of Fermi speeds, $\delta v \propto \alpha$.

3. Spin-orbit coupling and magnetization

Here, we consider a wire along x with a Zeeman field B_y and Rashba spin-orbit coupling λ. Its Hamiltonian is

$$H = \frac{k^2}{2m} - \mu + \lambda k \sigma_y - \gamma \mu_B B_y \frac{\sigma_y}{2}, \tag{A9}$$

where γ and μ_B are the gyromagnetic ratio and Bohr magneton, respectively, and $\sigma_y = \pm 1$ refers to spin along y. For each value of σ_y, there exists a right mover and a left mover at the Fermi level, resulting in a total of four Fermi points. For this system, there are two ways to obtain a symmetric band structure. The first is by switching off the magnetic field ($B_y = 0$), which yields two pairs of equal and opposite Fermi momenta:

$$|k_F| = m \left| -\sigma_y \lambda \pm \sqrt{\lambda^2 + \frac{2\mu}{m}} \right|, \tag{A10}$$

and equal Fermi speeds

$$v_F = \sqrt{\lambda^2 + \frac{2\mu}{m}}. \tag{A11}$$

In this case, band symmetry exists between a right-mover with spin σ_y and left-mover with spin $-\sigma_y$ due to $\mathcal{T}$. The second way to obtain a symmetric dispersion is by suppressing spin-orbit coupling ($\lambda = 0$). This, too, gives a pair of equal and opposite Fermi momenta for each value of σ_y due to $\mathcal{I}$:

$$K_{F,\sigma_y} = \sqrt{m(2\mu + \gamma \mu_B B_y \sigma_y)}, \tag{A12}$$

and equal Fermi speeds

$$V_{F,\sigma_y} = \sqrt{\frac{2\mu + \gamma \mu_B B_y \sigma_y}{m}}, \tag{A13}$$

When both B_y and λ are non-zero, neither the Fermi points nor the velocities appear in equal and opposite pairs. Their values now are,

$$k_{\sigma_y}^{R/L} = m \left(-\sigma_y \lambda + \sqrt{\lambda^2 + \frac{2\mu + \sigma_y \gamma \mu_B B_y}{m}} \right), \tag{A14}$$

$$v_{\sigma_y}^{R/L} = \sqrt{\lambda^2 + \frac{2\mu + \sigma_y \gamma \mu_B B_y}{m}}, \tag{A15}$$

Appendix B: Detailed calculation of $\sigma^{\mathbf{WL}}$

1. Self-energy

We consider a disorder potential $U(x) = \sum_n \mathcal{U}(x - R_n)$ with $\bar{U(x)} = 0$ and $U(x)\bar{U}(x') = n_i u_0^2 \delta(x - x')$ where the bar denotes disorder-average and n_i is the impurity density, and begin the analysis by considering the effect of band asymmetry on the self-energy as a function of complex frequency $\Sigma(z)$ [54, 55]:

$$\Sigma(z) = n_i u_0^2 \int_{-\pi}^{\pi} \frac{dk}{2\pi} \frac{1}{z - \epsilon_k}, \tag{B1}$$

Analytically continuing z within a half-plane, $z \to \varepsilon + i0^+\mathrm{sgn}[\mathrm{Im}(z)]$ and absorbing $\mathrm{Re}\Sigma$ into a redefinition of μ, we get a lifetime from the imaginary part:

$$\frac{1}{\tau(\varepsilon)} = 2\pi n_i u_0^2 \int_k \delta(\varepsilon - \epsilon_k) \tag{B2}$$

To simplify the analysis, let us assume there is a single left-mover at each ε with speed $v_L(\varepsilon)$ and a single right-mover with speed $v_R(\varepsilon)$. Then,

$$\frac{1}{\tau(\varepsilon)} = n_i u_0^2 \left(\frac{1}{v_L(\varepsilon)} + \frac{1}{v_R(\varepsilon)} \right), \tag{B3}$$

where substituting the density of states per unit length $g(\varepsilon) = \frac{1}{2\pi}\left(\frac{1}{v_L(\varepsilon)} + \frac{1}{v_R(\varepsilon)}\right)$, we get:

$$\frac{1}{\tau_0(\varepsilon)} = 2\pi n_i u_0^2 g(\varepsilon) \tag{B4}$$

Clearly, the Born lifetime depends only on the mean inverse speed and is not affected qualitatively by the velocity asymmetry. Nevertheless, it is convenient to separate the speeds into their average and differences, $v_L = v - \delta v/2$, $v_R = v + \delta v/2$. This gives

$$\frac{1}{\tau_0(\varepsilon)} = \frac{2 n_i u_0^2 v(\varepsilon)}{v^2(\varepsilon) - \delta v^2(\varepsilon)/4} \tag{B5}$$

Here, $G^R(k,\varepsilon)$, $G^A(k,\varepsilon)$, and $\mathcal{G}(k, i\nu_n)$ are the usual retarded, advanced, and Matsubara electron Green's functions.

2. Cooperon propagator

To determine the weak localization correction to the conductivity, $\sigma^{\mathrm{WL}}(\tilde{q})$, we need to calculate the polarization bubble due to the maximally crossed or Langer-Neal diagrams that capture constructive interference between time-reversed paths [54, 55]. The bubble is given by

$$\Pi^{WL}(\tilde{q}) = -\int_{\tilde{k},\tilde{k}'} v_{k+q/2} v_{k'+q/2} \mathcal{G}(\tilde{k}) \mathcal{G}(\tilde{k}+\tilde{q}) \mathcal{C}(\tilde{k},\tilde{k}',\tilde{q}) \mathcal{G}(\tilde{k}') \mathcal{G}(\tilde{k}'+\tilde{q}), \tag{B6}$$

where $\tilde{k} \equiv (k, i\nu_n)$, $\tilde{q} \equiv (q, i\omega_n)$, $\int_{\tilde{k}} \equiv T\sum_{ik_n} \int \frac{dk}{2\pi}$, and $\mathcal{C}$ is the resummed Cooperon propagator that is represented diagrammatically by a sum of parallel impurity lines [Fig. 1 (a,b)]. We use the notation $\mathcal{C}(\tilde{k},\tilde{k}',\tilde{q})$, where $\tilde{k}$ and $\tilde{k}'$ label the top incoming and outgoing lines while $\tilde{q}$ is the difference between the frequency/momentum of the bottom outgoing line and the top incoming line.

Some simplifications occur or can be justifiably made while doing these calculations. Since we will eventually be interested in the dc limit, so we can set $q = 0$. Also, impurity lines after disorder-averaging behave like interactions that conserve frequency, so the top and bottom fermion lines have frequencies $i\nu_n$ and $i\nu_n + i\omega_n$ for every diagram in the Dyson series for $\mathcal{C}$, or in short, $\mathcal{C} \propto \frac{1}{T}\delta_{\nu_n,\nu_n'}$. Finally, for short-range impurities, the scattering potential is momentum-independent. This ensures that $C(k,k',q=0)$ only depends on $k+k' \equiv Q$.

The Dyson series for $\mathcal{C}$ can now be resummed, and yields:

$$\mathcal{C}(Q; i\nu_n + i\omega_n, i\nu_n) = \frac{n_i^2 u_0^4 \int_p \mathcal{G}(Q-p, i\nu_n + i\omega_n)\mathcal{G}(p, i\nu_n)}{1 - n_i u_0^2 \int_p \mathcal{G}(Q-p, i\nu_n + i\omega_n)\mathcal{G}(p, i\nu_n)}, \tag{B7}$$

where we have written the frequency and momentum arguments separately in the Green's functions.

3. Contour integrals

This calculation can be carried out in two steps.

a. Frequency integral

Since two complex frequencies are involved, there are two branch cuts, at $\mathrm{Im}z = 0$, and $\mathrm{Im}z = -i\omega_n$ where $i\nu_n \to z$. We first perform the frequency integration by summing over one of the two frequencies ($i\nu_n$), doing a Taylor expansion around the other (ω), and calculating the correction to the conductivity [54, 55], $\sigma^{\mathrm{WL}} = -\lim_{\omega\to 0}\frac{1}{\omega}\mathrm{Im}\Pi^{\mathrm{WL}}(\omega)$. This gives

$$\sigma^{\mathrm{WL}} = -\int\limits_{k,k',\varepsilon} v_k v_{k'} f'(\varepsilon)\left[G^A(k,\varepsilon)G^A(k',\varepsilon)C^{RA}(Q;\varepsilon,\varepsilon) - G^R(k,\varepsilon)G^R(k',\varepsilon)C^{RR}(Q;\varepsilon,\varepsilon)\right]G^R(k',\varepsilon)G^R(k,\varepsilon) \tag{B8}$$

where

$$C^{RA}(Q;\varepsilon,\varepsilon) = \mathcal{C}(Q;\varepsilon+i0^+,\varepsilon-i0^+) = \frac{n_i^2u_0^4\int_p G^R(Q-p,\varepsilon)G^A(p,\varepsilon)}{1-n_iu_0^2\int_p G^R(Q-p,\varepsilon)G^A(p,\varepsilon)} = \frac{n_iu_0^2\zeta^{RA}(Q)}{1-\zeta^{RA}(Q)} \tag{B9}$$

$$C^{RR}(Q;\varepsilon,\varepsilon)C^{RR}(Q) = \mathcal{C}(Q;\varepsilon+i0^+,\varepsilon+i0^+) = \frac{n_i^2u_0^4\int_p G^R(Q-p,\varepsilon)G^R(p,\varepsilon)}{1-n_iu_0^2\int_p G^R(Q-p,\varepsilon)G^R(p,\varepsilon)} = \frac{n_iu_0^2\zeta^{RR}(Q)}{1-\zeta^{RR}(Q)} \tag{B10}$$

At $T\to 0$, $f'(\varepsilon)\to -\delta(\varepsilon)$, so only the point $\varepsilon = 0$ contributes. Suppressing ε in the arguments of G and C,

$$\sigma^{\mathrm{WL}} = 2\pi\int\limits_{k,k'} v_k v_{k'}\left[G^A(k)G^A(k')C^{RA}(Q) - G^R(k)G^R(k')C^{RR}(Q)\right]G^R(k')G^R(k) \tag{B11}$$

where $\varepsilon = 0$ is understood and $Q = k + k'$.

To evaluate $C^{RA}(Q)$ and $C^{RR}(Q)$, we need to evaluate $\zeta^{RA}(Q)$ and $\zeta^{RR}(Q)$. To account for inelastic scattering which leads to loss of phase coherence, we can phenomenologically modify $\zeta(Q)\to e^{-l/l_\phi}\zeta(Q)$, where l_ϕ is the phase coherence length and l is the mean free path. Physically, this allows a probability $\propto e^{l/l_\phi}$ for the particle to lose phase coherence between successive elastic scattering processes.

For symmetric metals, the dominant – in fact, divergent – contribution to $C^{RA}(Q)$ comes from $Q = 0$ because $\zeta^{RA}(Q=0)$ turns out to be 1 if $l/l_\phi\to 0$. In contrast, the 'RR' terms are expected to be subdominant.

b. Momentum integrals

After performing the frequency integral, we carry out the momentum integral for a general asymmetric dispersion which results in an expression involving the Fermi momenta of the two movers. We have

$$\zeta^{RA}(Q) = n_iu_0^2e^{-l/l_\phi}\int\frac{dp}{2\pi}\frac{1}{\epsilon_{Q-p}-\frac{i}{2\tau_0}}\frac{1}{\epsilon_p+\frac{i}{2\tau_0}} \tag{B12}$$

Now, there is no "special" value of Q where $\epsilon_p = \epsilon_{Q-p}$ over all p. Nonetheless, the dominant contribution will presumably come from terms where both p and $Q-p$ are close to Fermi points, k_F^R and $-k_F^L$, so the corresponding Q value is $Q_0 = k_F^R - k_F^L$. We have adopted a sign convention where $k_F^R, k_F^L > 0$ are the magnitudes of the Fermi momenta. Parametrizing (i) $p = k_F^R + P$, $Q-p = -k_F^L - P$, and (ii) $p = -k_F^L + P$, $Q-p = k_F^R - P$ gives

$$\zeta^{RA}(Q_0) = \frac{n_iu_0^2e^{-l/l_\phi}}{\pi}\int\limits_{-\infty}^{\infty}dP\frac{1}{v_LP-\frac{i}{2\tau_0}}\frac{1}{v_RP+\frac{i}{2\tau_0}}, \tag{B13}$$

where we have extended the limits of the P-integral cutoffs to $\pm\infty$ to focus on the contribution from regions near the Fermi points. In practice, the cutoffs will be determined by the non-linearity away from the Fermi points. This integral can be easily done by contour methods and gives

$$\zeta^{RA}(Q_0) = e^{-l/l_\phi}\left(1-\frac{\delta v^2}{4v^2}\right) \tag{B14}$$

Clearly, $\zeta_j^{RA} \approx 1$ for $\delta v \ll v$ and $l \ll l_\phi$. Importantly, $C^{RA}(Q_0) = \frac{n_i u_0^2 \zeta^{RA}(Q_0)}{1-\zeta^{RA}(Q_0)}$ no longer diverges for $l/l_\phi \to 0$ unlike the symmetric case.

Now, to calculate a more accurate result, we need to consider nearby momenta as well. For small deviations from Q_0, i.e., for $Q = Q_0 + \Delta Q$, the process can be repeated with (i) $p = k_F^R + P + \Delta Q/2$, $Q - p = -k_F^L - P + \Delta Q/2$, and (ii) $p = -k_F^L + P + \Delta Q/2$, $Q - p = k_F^R - P + \Delta Q/2$:

$$\zeta^{RA}(Q_0 + \Delta Q) = \frac{\zeta^{RA}(Q_0)}{1 + \left[e^{l/l_\phi}\tau_0 v \zeta^{RA}(Q_0)\Delta Q\right]^2} \tag{B15}$$

$$C^{RA}(Q_0 + \Delta Q) = \frac{\frac{v}{2\tau_0}\left[\zeta^{RA}(Q_0)\right]^2}{[1 - \zeta^{RA}(Q_0)] + \left[e^{l/l_\phi}\tau_0 v \zeta^{RA}(Q_0)\Delta Q\right]^2} \tag{B16}$$

where we have used Eq. (B5) with $\varepsilon = 0$. Compared to a symmetric dispersion which has $Q_0 = 0$, $\zeta^{RA}(Q_0) = 1$ and hence, a double pole in C^{RA} at $Q = 0$, $C^{RA}(Q_0 + \Delta Q)$ has poles away from the real axis at

$$\Delta Q = \pm i \frac{\sqrt{1 - \zeta^{RA}(Q_0)}}{e^{l/l_\phi}\tau_0 v \zeta^{RA}(Q_0)} \tag{B17}$$

Similarly,

$$\zeta^{RR}(Q_0 + \Delta Q) = e^{-l/l_\phi}\frac{n_i u_0^2}{2\pi} 2\mathrm{Re} \int_{-\infty}^{\infty} dP \left(\frac{1}{v_L(P - \Delta Q/2) + \frac{i}{2\tau_0}} \frac{1}{v_R(P + \Delta Q/2) + \frac{i}{2\tau_0}} \right) \tag{B18}$$

Now, both poles are above the real axis, so completing the contour in the lower half-plane causes the integral to vanish exactly. Thus, $\zeta^{RR}(Q_0 + \Delta Q) = C^{RR}(Q_0 + \Delta Q) = 0$.

4. Final result for σ^{WL}

With the expression obtained after frequency and momentum integral, we can calculate the correction to conductivity by doing another momentum integral. Explicitly,

$$\sigma^{\mathrm{WL}} = 2\pi \int_{k,k'} v_k v_{k'} \frac{1}{\epsilon_k^2 + \frac{1}{4\tau_0^2}} \frac{1}{\epsilon_{k'}^2 + \frac{1}{4\tau_0^2}} C^{RA}(k + k') \tag{B19}$$

Again, we focus on pairs (k, k') such that $k + k' = Q_0 + \Delta Q$, i.e., k and k' are near the left and right Fermi points or vice versa. Parameterizing (i) $k = k_F^R + K + \Delta Q/2$, $k' = -k_F^L - K + \Delta Q/2$, and (ii) $k = -k_F^L + K + \Delta Q/2$, $k' = k_F^R - K + \Delta Q/2$,

$$\sigma^{\mathrm{WL}} = -2\pi \int_{K,\Delta Q} v_L v_R \left[\frac{1}{v_R^2(K + \Delta Q/2)^2 + \frac{1}{4\tau_0^2}} \frac{1}{v_L^2(K - \Delta Q/2)^2 + \frac{1}{4\tau_0^2}} + (\Delta Q \to -\Delta Q) \right] C^{RA}(Q_0 + \Delta Q) \tag{B20}$$

For complex K, the above integral has simple poles at $K = \pm\frac{Q}{2} \pm \frac{i}{2v_{L,R}\tau_0}$. Completing the K-contour in, say, the upper half plane gives

$$\sigma^{\mathrm{WL}} = -2\pi \int_{\Delta Q} \frac{4\tau_0^3 v e^{l/l_\phi}\zeta^{RA}(Q_0)}{1 + \left[e^{l/l_\phi}\tau_0 v \zeta^{RA}(Q_0)\Delta Q\right]^2} C^{RA}(Q_0 + \Delta Q) \tag{B21}$$

Besides the two simple poles of $C^{RA}(Q_0 + \Delta Q)$ given by Eq. (B17), we now have another pair of simple poles at $\Delta Q = \pm i \left[e^{l/l_\phi}\tau_0 v \zeta^{RA}(Q_0)\right]^{-1}$. Integrating over a complex half-plane gives

$$\sigma^{\mathrm{WL}} = -\frac{2\pi\tau_0 v \left[\zeta^{RA}(Q_0)\right]^2}{\left[\sqrt{1 - \zeta^{RA}(Q_0)} + 1 - \zeta^{RA}(Q_0)\right]} \tag{B22}$$

For large inelastic mean free path ($l \ll l_\phi$) and small asymmetry ($|\delta v| \ll v$), using Eq. (B14) and reinstating dimensionful factors of e^2 and $\hbar$ gives Eq. (1) in the main paper to leading orders in l/l_ϕ and $\delta v/v$.

Appendix C: Recursive Green's function method

Recursive Green's function method is an iterative algorithm for calculating properties of the system such as the localization length in the thermodynamic limit [57–59]. As the name suggests, this method calculates the Green's function recursively by using that of a smaller system size and growing the system layer-by-layer.

For a given Hamiltonian $H(N)$ for a system size of N, the Green's function at complex energy z, $G(z, N)$ is defined as its resolvent and for a real energy E, it is obtained by taking the imaginary part of z to zero. The localization length (ξ) in terms of the matrix elements of the Green's function is

$$\frac{4}{\xi} = -\lim_{n\to\infty} \frac{1}{n} \ln\left(\mathrm{Tr}|G_{1,n}|^2\right), \tag{C1}$$

where $G_{n,m} \equiv \langle n|G(z,m)|m\rangle$.

The quantity $A_n = G^{-1}_{1,n-2}$, obeys the recursive relation [58]:

$$A_{n+2} = (E - H_{n+1})V_n^{-1}A_{n+1} - V_n^{\dagger}V_{n-1}A_n, \tag{C2}$$

where H_n is the matrix representing the tight-binding Hamiltonian for the n^{th} slice, and V_n is the matrix that describes the particles hopping onto the $(n+1)^{th}$ slice from the n^{th} slice. For our model [Fig. 2], we have,

$$H_n = \begin{bmatrix} \epsilon_i & t \\ t & \epsilon_{i+1} \end{bmatrix}, V_{n,n+1} = \begin{bmatrix} t'e^{-i\theta} & t \\ 0 & t'e^{-i\theta} \end{bmatrix}. \tag{C3}$$

ξ can be calculated by iterating Eq. (C2) with some initial values for A_0 and A_1, which we choose as $A_0 = 0, A_1 = V_0$. However, Eq. (C2) suffers from a numerical instability in that the elements of A_n grow exponentially for large n and hence require some regularization. Therefore, in every iteration we multiply both sides of Eq. (C2) with $[A_{n+1}]^{-1}$. Simplifying this procedure, we get the regularized recursion relation [58],

$$\tilde{A}_n = (E - H_{n+1})V_n^{-1} - V_n^{\dagger}V_{n-1}^{-1}\tilde{A}_{n-1}^{-1}, \tag{C4}$$

that helps us resolve this issue and calculate ξ. We choose $\tilde{A}_0 = 1$ and to calculate ξ, define a new matrix,

$$B_n = \frac{B_{n-1}\tilde{A}_n^{-1}}{b_n}, \tag{C5}$$

where $b_n = ||B_n||$ is the Frobenius norm of B_n, and $B_0 = 1$. We calculate B_n and store b_n in every iteration of Eq. (C4). The matrix B_n is very useful because

$$\ln\left(\mathrm{Tr}|G_{1,n}|^2\right) = 2\left[\ln(b_{n+1}) + \cdots + \ln(b_1)\right], \tag{C6}$$

which can then be substituted in Eq. (C1) to determine ξ.

[1] B. Kramer and A. MacKinnon, Reports on Progress in Physics **56**, 1469 (1993).

[2] E. Abrahams, P. W. Anderson, D. C. Licciardello, and T. V. Ramakrishnan, Phys. Rev. Lett. **42**, 673 (1979).

[3] P. W. Anderson, E. Abrahams, and T. V. Ramakrishnan, Phys. Rev. Lett. **43**, 718 (1979).

[4] G. Bergmann, Physics Reports **107**, 1 (1984).

[5] B. L. Altshuler, D. Khmel'nitzkii, A. I. Larkin, and P. A. Lee, Phys. Rev. B **22**, 5142 (1980).

[6] E. Akkermans and G. Montambaux, *Mesoscopic Physics of Electrons and Photons* (Cambridge University Press, 2007).

[7] P. W. Anderson, Phys. Rev. **109**, 1492 (1958).

[8] D. S. Wiersma, P. Bartolini, A. Lagendijk, and R. Righini, Nature **390**, 671 (1997).

[9] A. A. Chabanov, M. Stoytchev, and A. Z. Genack, Nature **404**, 850 (2000).

[10] M. Segev, Y. Silberberg, and D. N. Christodoulides, Nature Photonics **7**, 197 (2013).
[11] R. Weaver, Wave Motion **12**, 129 (1990).
[12] H. Hu, A. Strybulevych, J. H. Page, S. E. Skipetrov, and B. A. van Tiggelen, Nature Physics **4**, 945 (2008).
[13] J. Chabé, G. Lemarié, B. Grémaud, D. Delande, P. Szriftgiser, and J. C. Garreau, Phys. Rev. Lett. **101**, 255702 (2008).
[14] G. Semeghini, M. Landini, P. Castilho, S. Roy, G. Spagnolli, A. Trenkwalder, M. Fattori, M. Inguscio, and G. Modugno, Nature Physics **11**, 554 (2015).
[15] J. Billy, V. Josse, Z. Zuo, A. Bernard, B. Hambrecht, P. Lugan, D. Clément, L. Sanchez-Palencia, P. Bouyer, and A. Aspect, Nature **453**, 891 (2008).
[16] A. Aspect and M. Inguscio, Physics Today **62**, 30 (2009).
[17] A. Alexandru, P. F. Bedaque, and S. Lawrence, Phys. Rev. A **101**, 032325 (2020).
[18] A. Lagendijk, B. van Tiggelen, and D. S. Wiersma, Physics Today **62**, 24 (2009).
[19] P. A. Lee and T. V. Ramakrishnan, Rev. Mod. Phys. **57**, 287 (1985).
[20] F. Evers and A. D. Mirlin, Rev. Mod. Phys. **80**, 1355 (2008).
[21] A. Altland and M. R. Zirnbauer, Phys. Rev. B **55**, 1142 (1997).
[22] E. P. Wigner, Mathematical Proceedings of the Cambridge Philosophical Society **47**, 790 (1951).
[23] F. J. Dyson, Journal of Mathematical Physics **3**, 1199 (1962).
[24] S. Hikami, A. I. Larkin, and Y. Nagaoka, Progress of Theoretical Physics **63**, 707 (1980).
[25] J. Alicea, Reports on Progress in Physics **75** (2012), 10.1088/0034-4885/75/7/076501.
[26] C. W. J. Beenakker, Annual Review of Condensed Matter Physics **4**, 113 (2013).
[27] A. Y. Kitaev, Physics-Uspekhi **44**, 131 (2001).
[28] R. M. Lutchyn, E. P. A. M. Bakkers, L. P. Kouwenhoven, P. Krogstrup, C. M. Marcus, and Y. Oreg, Nature Reviews Materials **3**, 52 (2018).
[29] R. M. Lutchyn, J. D. Sau, and S. Das Sarma, Phys. Rev. Lett. **105**, 77001 (2010).
[30] F. Ando, Y. Miyasaka, T. Li, J. Ishizuka, T. Arakawa, Y. Shiota, T. Moriyama, Y. Yanase, and T. Ono, Nature **584**, 373 (2020).
[31] A. Daido, Y. Ikeda, and Y. Yanase, Phys. Rev. Lett. **128**, 037001 (2022).
[32] J.-X. Lin, P. Siriviboon, H. D. Scammell, S. Liu, D. Rhodes, K. Watanabe, T. Taniguchi, J. Hone, M. S. Scheurer, and J. I. A. Li, "Zero-field superconducting diode effect in small-twist-angle trilayer graphene," (2021).
[33] Y.-Y. Lyu, J. Jiang, Y.-L. Wang, Z.-L. Xiao, S. Dong, Q.-H. Chen, M. V. Milošević, H. Wang, R. Divan, J. E. Pearson, P. Wu, F. M. Peeters, and W.-K. Kwok, Nature Communications **12**, 2703 (2021).
[34] H. Narita, J. Ishizuka, R. Kawarazaki, D. Kan, Y. Shiota, T. Moriyama, Y. Shimakawa, A. V. Ognev, A. S. Samardak, Y. Yanase, and T. Ono, Nature Nanotechnology **17**, 823 (2022).
[35] J. Shin, S. Son, J. Yun, G. Park, K. Zhang, Y. J. Shin, J.-G. Park, and D. Kim, "Magnetic proximity-induced superconducting diode effect and infinite magnetoresistance in van der waals heterostructure," (2021).
[36] N. F. Q. Yuan and L. Fu, Proceedings of the National Academy of Sciences **119**, e2119548119 (2022), https://www.pnas.org/doi/pdf/10.1073/pnas.2119548119.
[37] R. Wakatsuki, Y. Saito, S. Hoshino, Y. M. Itahashi, T. Ideue, M. Ezawa, Y. Iwasa, and N. Nagaosa, Science Advances **3** (2017), 10.1126/sciadv.1602390.
[38] R. Wakatsuki and N. Nagaosa, Physical Review Letters **121**, 26601 (2018), arXiv:1712.02086.
[39] Y. Miyasaka, R. Kawarazaki, H. Narita, F. Ando, Y. Ikeda, R. Hisatomi, A. Daido, Y. Shiota, T. Moriyama, Y. Yanase, and T. Ono, Applied Physics Express **14**, 073003 (2021).
[40] B. Zhai, B. Li, Y. Wen, F. Wu, and J. He, Phys. Rev. B **106**, L140505 (2022).
[41] A. Daido and Y. Yanase, Phys. Rev. B **106**, 205206 (2022).
[42] C. Baumgartner, L. Fuchs, A. Costa, S. Reinhardt, S. Gronin, G. C. Gardner, T. Lindemann, M. J. Manfra, P. E. Faria Junior, D. Kochan, J. Fabian, N. Paradiso, and C. Strunk, Nature Nanotechnology **17**, 39 (2022).
[43] C. Baumgartner, L. Fuchs, A. Costa, J. Picó-Cortés, S. Reinhardt, S. Gronin, G. C. Gardner, T. Lindemann, M. J. Manfra, P. E. F. Junior, D. Kochan, J. Fabian, N. Paradiso, and C. Strunk, Journal of Physics: Condensed Matter **34**, 154005 (2022).
[44] M. Davydova, S. Prembabu, and L. Fu, Science Advances **8**, eabo0309 (2022), https://www.science.org/doi/pdf/10.1126/sciadv.abo0309.
[45] J. Diez-Merida, A. Diez-Carlon, S. Y. Yang, Y. M. Xie, X. J. Gao, K. Watanabe, T. Taniguchi, X. Lu, K. T. Law, and D. K. Efetov, "Magnetic josephson junctions and superconducting diodes in magic angle twisted bilayer graphene," (2021).
[46] B. Pal, A. Chakraborty, P. K. Sivakumar, M. Davydova, A. K. Gopi, A. K. Pandeya, J. A. Krieger, Y. Zhang, M. Date, S. Ju, N. Yuan, N. B. M. Schröter, L. Fu, and S. S. P. Parkin, Nature Physics (2022), 10.1038/s41567-022-01699-5.
[47] H. Wu, Y. Wang, Y. Xu, P. K. Sivakumar, C. Pasco, U. Filippozzi, S. S. P. Parkin, Y.-J. Zeng, T. McQueen, and M. N. Ali, Nature **604**, 653 (2022).
[48] K. Halterman, M. Alidoust, R. Smith, and S. Starr, Phys. Rev. B **105**, 104508 (2022).
[49] Y. Zhang, Y. Gu, P. Li, J. Hu, and K. Jiang, Phys. Rev. X **12**, 041013 (2022).
[50] D. Wang, Q.-H. Wang, and C. Wu, "Symmetry constraints on direct-current josephson diodes," (2022).
[51] A. V. Samokhvalov, A. A. Kopasov, A. G. Kutlin, S. V. Mironov, A. I. Buzdin, and A. S. Mel'nikov, JETP Letters **113**, 34 (2021).
[52] S. Mironov and A. Buzdin, Phys. Rev. Lett. **118**, 077001 (2017).

[53] P. Hosur and D. Palacios, "Equilibrium supercurrent in proximity-induced superconductors due to band asymmetry," (2022).
[54] H. Bruus and K. Flensberg, *Many-body quantum theory in Condensed matter physics an introduction* (Oxford University Press, 2020).
[55] P. Coleman, *Introduction to many-body physics* (Cambridge University Press, 2019).
[56] R. Sepehrinia and A. Sheikhan, Computing in Science & Engineering **13**, 74 (2011).
[57] D. J. Thouless and S. Kirkpatrick, Journal of Physics C: Solid State Physics **14**, 235 (1981).
[58] A. Kosior, J. Major, M. Płodzień, and J. Zakrzewski, Phys. Rev. A **92**, 023606 (2015).
[59] A. MacKinnon and B. Kramer, Phys. Rev. Lett. **47**, 1546 (1981).
[60] D. J. THOULESS, in *Ill-Condensed Matter* (CO-PUBLISHED WITH NORTH-HOLLAND PUBLISHING CO., 1984) pp. 1–62.
[61] D. Liang, M. R. Sakr, and X. P. A. Gao, Nano Letters **9**, 1709 (2009).
[62] C. W. J. Beenakker and H. van Houten, Phys. Rev. B **38**, 3232 (1988).
[63] F. A. An, E. J. Meier, and B. Gadway, Phys. Rev. X **8**, 031045 (2018).
[64] M. Aidelsburger, M. Atala, S. Nascimbène, S. Trotzky, Y.-A. Chen, and I. Bloch, Phys. Rev. Lett. **107**, 255301 (2011).
[65] P. Weinberg and M. Bukov, SciPost Phys. **2**, 003 (2017).
[66] P. Weinberg and M. Bukov, SciPost Phys. **7**, 020 (2019).